The Astrophysical Journal, 423:L59–L62, 1994 March 1

COMPARATIVE ANALYSIS OF THE FAR-INFRARED AND ^{13}CO ($J = 0$–1) EMISSIONS OF THE TAURUS COMPLEX

Alain Abergel and François Boulanger
IAS, Bâtiment 121, 91405 Orsay, France

and

Akira Mizuno and Yasuo Fukui
Radio Astronomy Laboratory, Department of Physics and Astrophysics, Nagoya University, Chikusaka-ku Nagoya 464-01 Japan

Received 1993 May 25; accepted 1993 October 18

ABSTRACT

IRAS images of the Taurus complex are presented. The map of the cold IR emission, emission with a low 60–100 μm color ratio, is dominated by a spectacular network of filament-like structures, with a typical width equal to ∼1 pc, including almost all star-forming regions.

Comparable in angular resolution with the *IRAS* data, the velocity-integrated ^{13}CO ($J = 1$–0) molecular map of the Taurus region obtained by Fukui & Mizuno (1991) at Nagoya (Japan) is strongly correlated with the cold component of the IR emission maps. We have analyzed the correlation inside small boxes whose size is 0.9 pc. The slope of regression line between the two emissions goes from 0.8 to 1.4 MJy sr^{-1} K^{-1} km^{-1} s. Moreover, slope gradients are visible within given structures.

Independent conversions of the ^{13}CO ($J = 1$–0) and the cold component emissions into H_2 column densities show that the ^{13}CO and cold component emitting volumes are roughly comparable. This could explain the correlation and the limited range of values found for the regression line slope between the two emissions.

The slope variations of a factor of ∼2 with distances as small as our analysis box, i.e., 0.9 pc, should result from different physical properties of the dust or differences in ^{13}CO abundance, excitation, and radiation transfer conditions.

Subject headings: ISM: clouds — ISM: molecules

1. INTRODUCTION

The large-scale structure of dark molecular clouds can mainly be studied from *IRAS* data obtained at four wavelengths (12, 25, 60, and 100 μm), and from the emission of the carbon monoxide and its isotopes, for different transitions. Each observation gives information about different components of the clouds, and the comparison of independent observations would allow to constrain our understanding of the distribution of matter inside molecular clouds.

Presently, only the *IRAS* observations give a complete spatial view at interstellar molecular clouds. Molecular surveys with comparable resolution have limited extents, and are often biased toward regions of high visible extinction.

The origin of the emission into the four *IRAS* bands has been discussed in detail by Désert, Boulanger, & Puget (1990). The emission at 100 μm comes from large grains mixed with the gas and traces matter illuminated by the radiation field of the galaxy irrespective of its chemical composition (i.e., atomic or molecular gas). The *IRAS* color has been shown to widely vary within nearby molecular complexes (Laurejis, Clark, & Prusti 1991; Boulanger et al. 1990). In the model of Désert et al. (1990), the high $I_\nu(60)/I_\nu(100)$ color ratio of the warm component is explained by a contribution of very small grains (VSGs) to about half of the 60 μm emission. The change in the $I_\nu(60)/I_\nu(100)$ color ratio between the warm and cold components could result from an increase in size of the VSGs by mantle formation (Laurejis et al. 1991), or mutual coagulation of grains. For this to happen the gas must be sufficiently dense. Under these conditions large grains are also likely to grow mantles and to accrete small particles. This may change their equilibrium temperature and also affect the $I_\nu(60)/I_\nu(100)$ color.

The photodissociation and the chemistry of interstellar CO are studied in detail by van Dishoeck & Black (1988) and Viala et al. (1988). The millimeter emissions of CO and its isotopes come from regions which are dense enough for the molecules to exist and to be collisionally excited. These molecules are protected from photodissociation by self-shielding, mutual shielding, shielding by coincident H and H_2 lines, and attenuation of radiation by dust particles and carbon atoms. The less abundant isotopes such as ^{13}CO and C^{18}O are likely to come from a smaller volume of the cloud than ^{12}CO. The abundance of ^{13}CO in dense clouds is difficult to model, because its value depends at least on two competing effects: the photodissociation and the formation of ^{13}CO from ^{13}C$^+$ and CO (fractionation).

The ^{12}CO ($J = 1$–0) emission becomes rapidly optically thick inside dense regions of molecular clouds and traces predominantly the external parts of clouds. The isotopic variant ^{13}CO is less abundant, and thus, its emission traces the cores of dark clouds. Inside the Taurus complex, Nercessian et al. (1988) have confirmed that the ^{13}CO emission appears "strongly correlated with the visual extinction."

The correlation between the far-IR and the ^{13}CO emissions has been previously studied in several dark clouds: Heiles' Cloud 2 (HCL 2) by Cernicharo & Guélin (1987), Barnard 5 (B5) by Langer et al. (1989), HCL 2 and Barnard 18 (B18) by Snell, Heyer, & Schloerb (1989), and Lynds 134 (L134) by Laurejis et al. (1991).

The goal of the present study is to extend these results to a molecular complex as a whole, using the *IRAS* data and the regularly sampled and unbiased surveys of Fukui & Mizuno (1991).

2. A LARGE-SCALE ANALYSIS OF THE COLD COMPONENT OF THE FAR-INFRARED EMISSION FROM THE TAURUS MOLECULAR CLOUD

As explained by Abergel et al. (1994), the *IRAS* data from the Taurus region for the four *IRAS* bands (12, 25, 60, and 100 μm) were co-added to produce four 8° × 8° images later mosaicked into 15° × 15° images with 1′ pixels and 4′ spatial resolution. Then the galactic and zodiacal emissions unrelated to the clouds have been removed. Figures 1*a* and 1*b* (Plates L6 and L7) show the 100 and 60 μm images obtained after the whole processing. The assumed distance of this cloud is equal to 140 pc, since Elias (1978). These images contain a lot of information which will not be all used in this paper.

Snell et al. (1989) have shown that the dust optical depth, computed from the 60 and 100 μm *IRAS* maps, is much better correlated with the velocity-integrated ^{13}CO emission than the 100 μm emission. Laurejis et al. (1991) have compared the far-infrared emission with the ^{13}CO emission in the Lynds 134 (L134) cloud complex. A low value of the correlation coefficient between the 100 μm emission and the velocity-integrated ^{13}CO emission was obtained, but this value spectacularly increased when the cold component of the far-infrared emission as defined below was compared to the ^{13}CO emission. Thus we shall now concentrate our study to the cold component emission.

The average color ratio $R(60, 100)$ of the whole map has been estimated to 0.15 by eye-fitting the 60–100 μm correlation diagram with a line, with a relative uncertainty of 10% because of the dispersion of the points. This value is inside the range determined by Boulanger et al. (1990) for a smaller (9° × 9°) map of the same region. The cold component of the dust emission was then computed according to the relationship (Fig. 2 [Pl. L8]):

$$I(\text{cold}) = I_\nu(100) - I_\nu(60)/0.15 .$$

In the cold emission map (Fig. 2) structures with contrast on small angular scale stand out. Much of these structures were not obvious in the original maps; the extended emission with a uniform color ratio (and equal to $\sim$0.15) has been removed. Variations of the zero level across the image may be partly related to the uncertainties of the zodiacal background, but none of the contrasted structures, warm or cold (negative or positive on Fig. 2), look like any of the zodiacal features described by Sykes (1988).

In the center of Figure 2, bright and small-scale structures predominantly elongated toward the northwest direction appears as a spectacular network of narrow filaments, with a typical width equal to $\sim$1 pc. They are due to a sharp increase of the 100 μm emission with no counterpart in the 60 μm emission. Such cold emission has been already identified inside L134 by Laurejis et al. (1991) and is also present in the northeast quarter of the Taurus image.

On the same image, regions with high 60 μm emission relative to the 100 μm emission appear dark, corresponding to warm pieces of clouds with $R(60, 100) \sim 0.2$. To the south of the image, the clouds are all warm but appear gray because of a locally positive zero level. Their morphology is not dominated by any filament-like network, as for the cold component. Quasi-point–like dark regions correspond to stars or embedded warm objects. Most of them have been listed by Beichman, Boulanger, & Moshir (1992) as *IRAS* faint sources corresponding to young protostellar objects. It is remarkable that all these objects are inside cold emission regions: star-forming regions are contained within cold emission regions.

3. A COMPARATIVE ANALYSIS OF THE FAR-INFRARED EMISSION AND THE ^{13}CO (J = 1–0) EMISSION IN THE TAURUS CLOUD

The velocity integrated ^{13}CO (J = 1–0) molecular maps obtained by Fukui & Mizuno (1991) with the 4 m millimeter telescope at Nagoya (Japan) are regularly sampled (2′), with a beam size equal to 3′. Thus these data are comparable in angular resolution with the *IRAS* data. The used map (Fig. 3 [Pl. L9]) is centered on the position: $l = 171°$, $b = -15.7°$, in Galactic coordinates (or $\alpha = 4^{\rm h}21^{\rm m}21^{\rm s}$, $\delta = 26^\circ\!.64$); its angular size is 10° × 5°, corresponding to 24 × 12 pc^2.

Several molecular condensations and two filament-like clouds with a tilt angle of $\sim$20° are visible. The 100 and 60 μm *IRAS* maps (Figs. 1*a* and 1*b*) and the cold component emission map (Fig. 2) have been projected upon the same grid that the one of the ^{13}CO map (see Figs. 4*a*, 4*b*, and 5 [Pls. L10–L12]). The spatial correlation between the ^{13}CO emission and the cold component of the dust emission is quite spectacular: all molecular condensations and filaments of the ^{13}CO map are visible on the cold component map. It is clear that the correlation between the cold component and the ^{13}CO emissions is much better than between the 100 μm (or the 60 μm) and the ^{13}CO emissions.

However, the correlation diagram ^{13}CO–cold component emissions (Fig. 6) show large scatter with similar amplitudes for all intensities (the value of the correlation coefficient is equal to 0.57), which has two origins: (1) the correlation law may change from region to region within the complex. (2) local heating due to embedded faint sources may warm up the surrounding dust, making the correlation worse. These sources are not detectable on the ^{13}CO map (Fig. 3) while the locally heated dust is visible as dark spots on the cold component map (Fig. 5).

In order to study the local correlation between the two emissions, we have analyzed the correlation inside small boxes with a size equal to 21 × 21 pixels, corresponding to 0.9 × 0.9 pc^2.

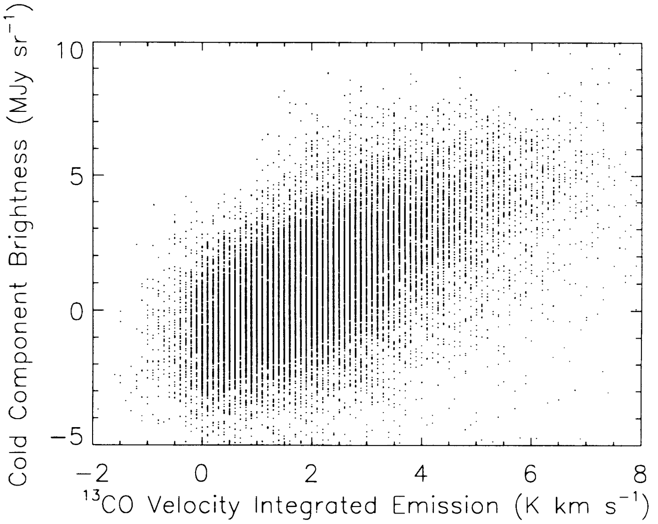

FIG. 6.—Cold component of the dust emission as a function of the ^{13}CO integrated emission, for each pixel position of Fig. 3. Pixels with negative cold component of the dust emission correspond to stars or embedded warm objects listed by Beichman et al. (1992).

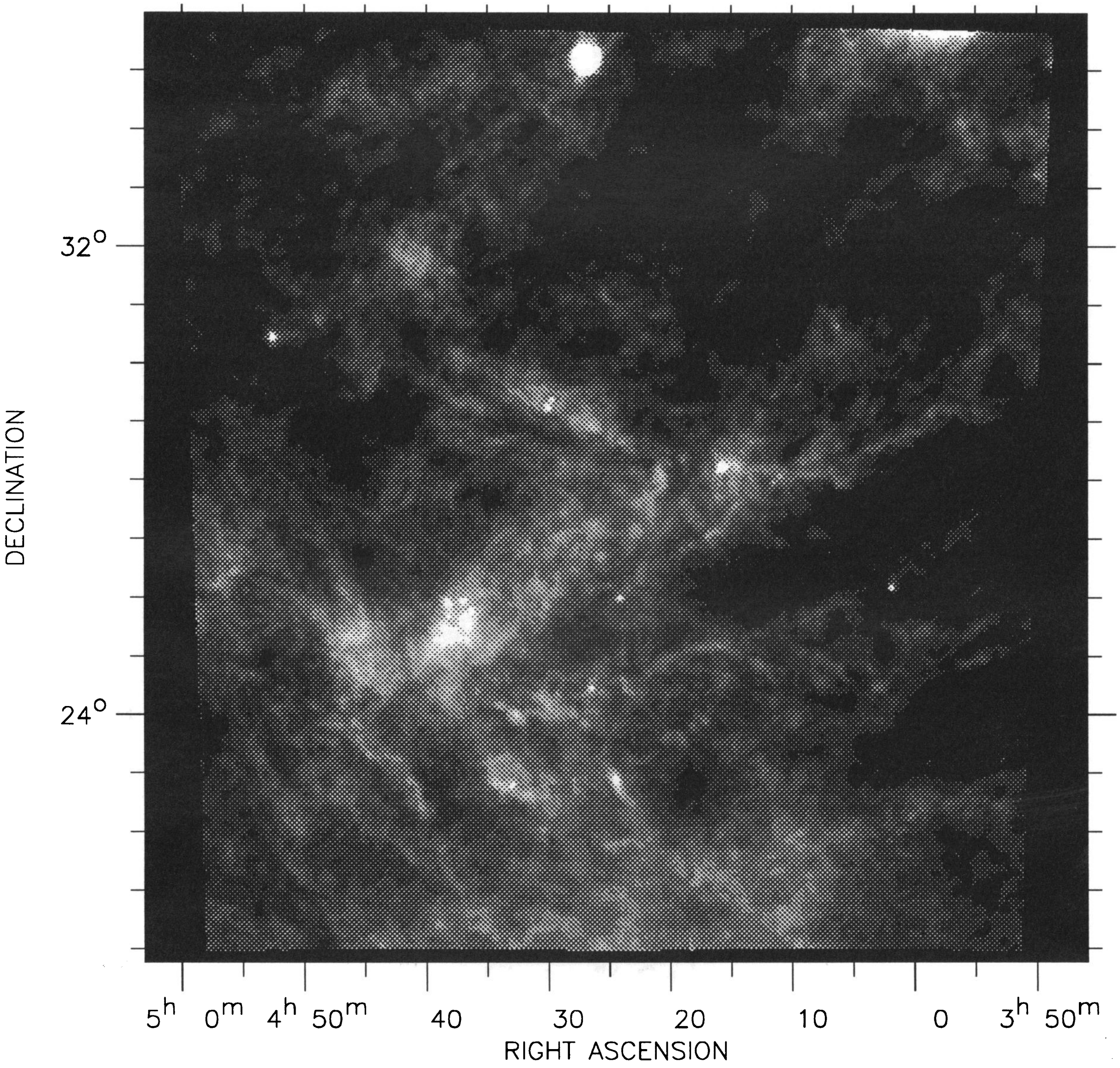

FIG. 1*a*

FIG. 1.—Large-scale (*a*) 100 μm and (*b*) 60 μm *IRAS* maps of the Taurus region after subtraction of the galactic and zodiacal emissions. Range: 100 μm: 0 to 30 MJy sr^{-1}. 60 μm: 0 to 5 MJy sr^{-1}.

ABERGEL et al. (see 423, L60)

1994ApJ...423L..59A

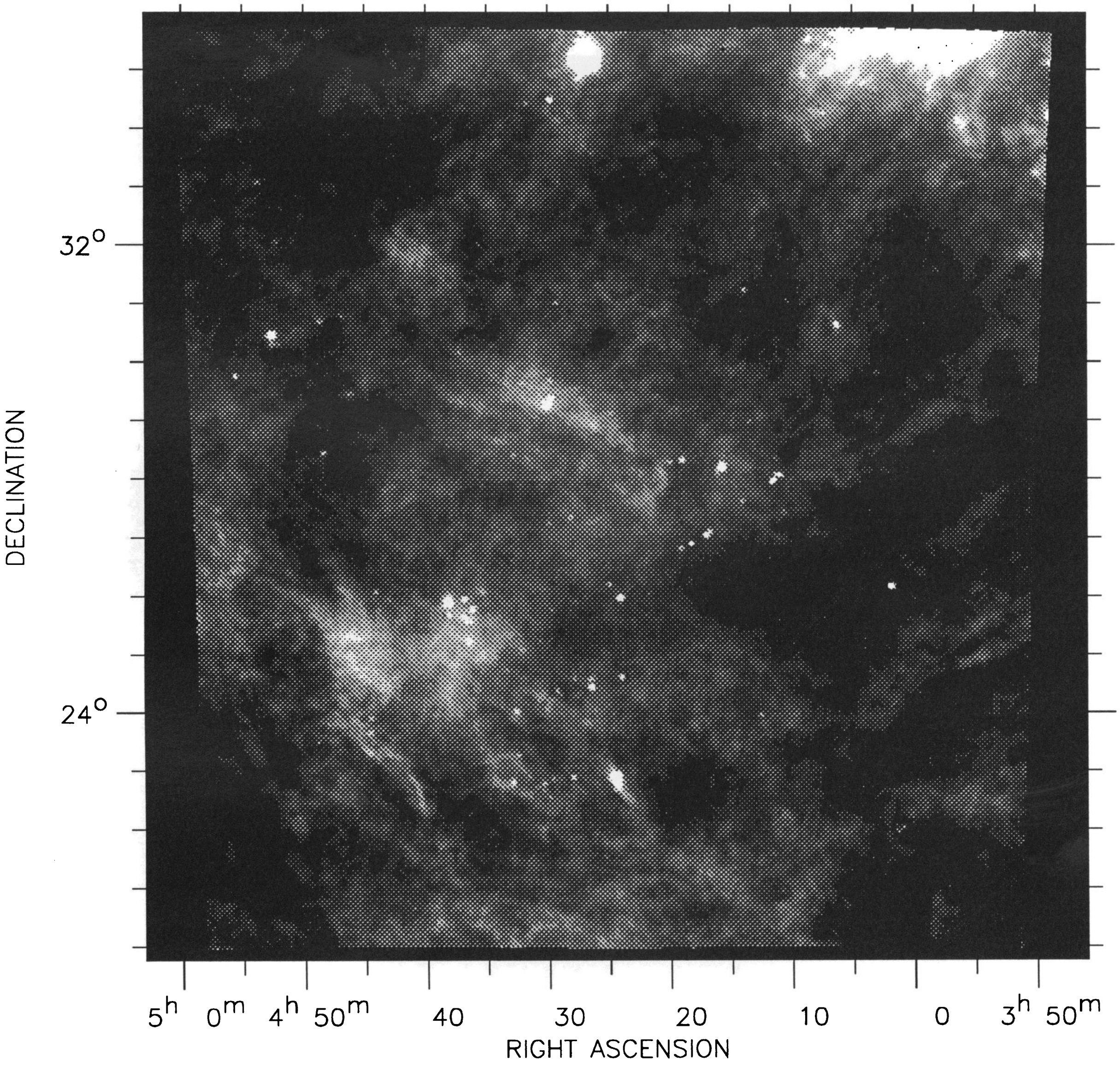

FIG. 1*b*

ABERGEL et al. (see 423, L60)

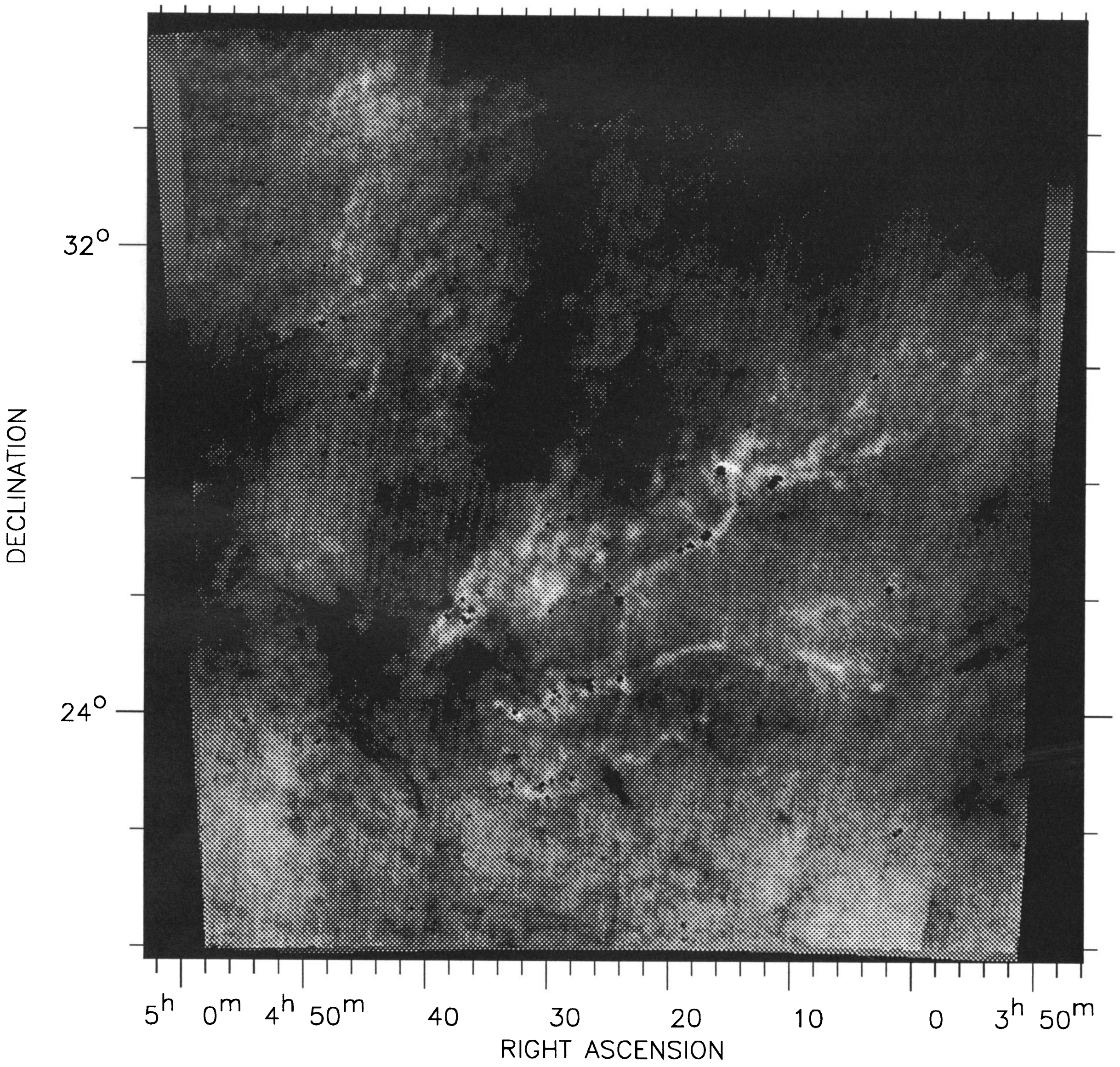

FIG. 2.—Large-scale cold component of the dust emission computed by subtracting from $I_\nu(100)$ the quantity $I_\nu(60)/0.15$. Range: -5 to 10 MJy sr^{-1}.

ABERGEL et al. (see 423, L60)

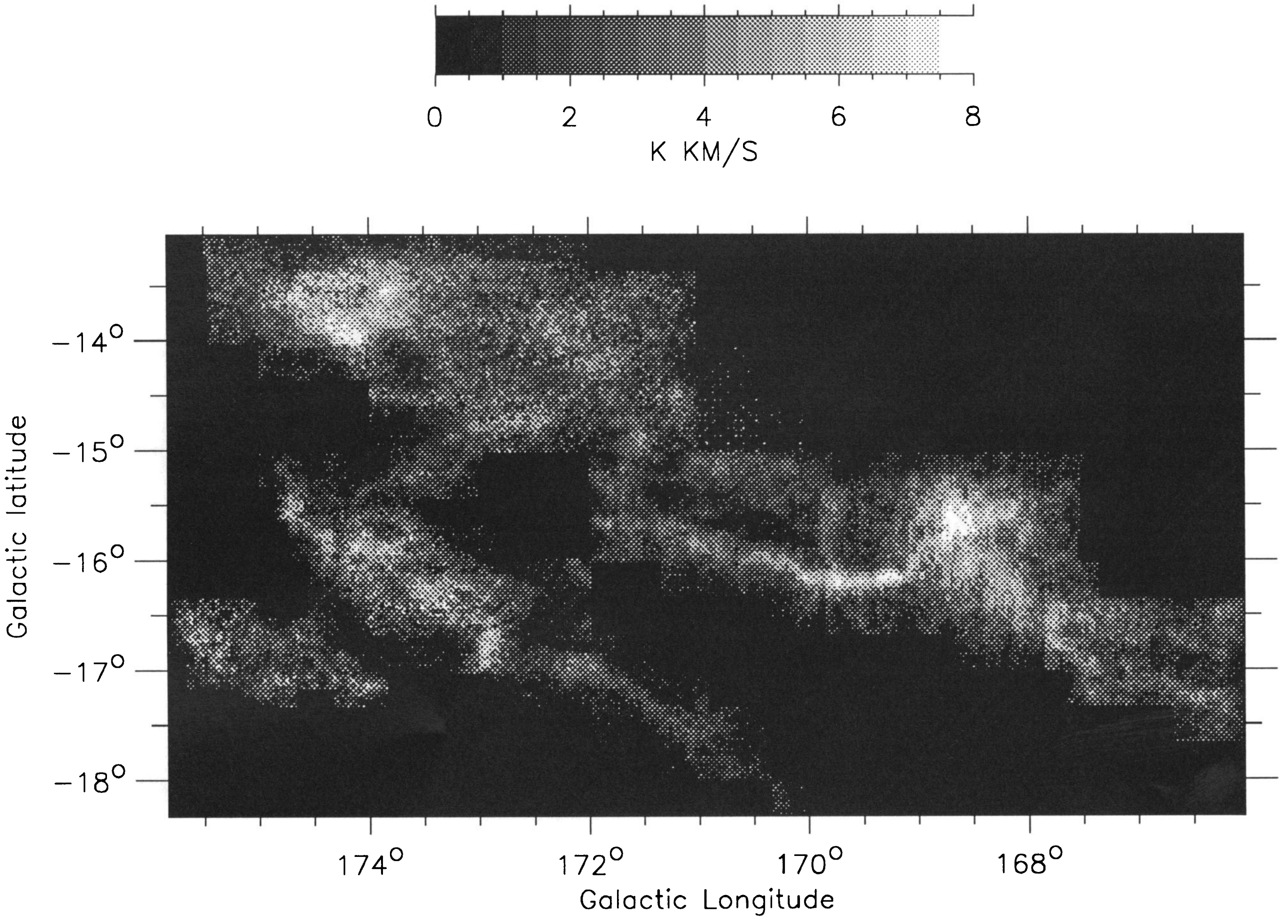

FIG. 3.—Total intensity map in ^{13}CO (J = 1–0) emission obtained with the 4 m millimeter telescope at Nagoya (Japan), from Fukui & Mizuno (1991)

ABERGEL et al. (see 423, L60)

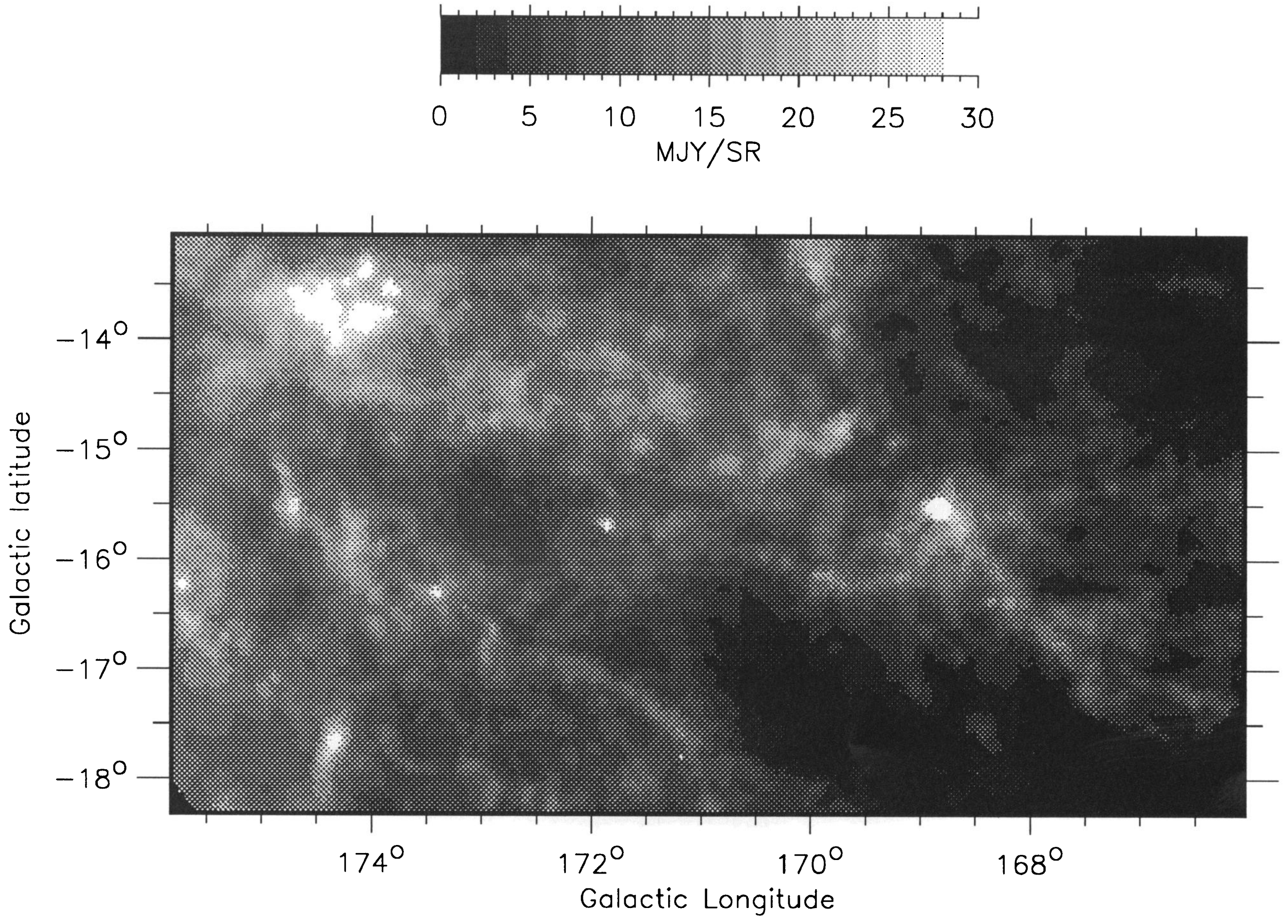

FIG. 4*a*

FIG. 4.—(*a*) 100 μm and (*b*) 60 μm *IRAS* maps projected upon the same grid that the one of the ^{13}CO (J = 1–0) map (Fig. 3)

ABERGEL et al. (see 423, L60)

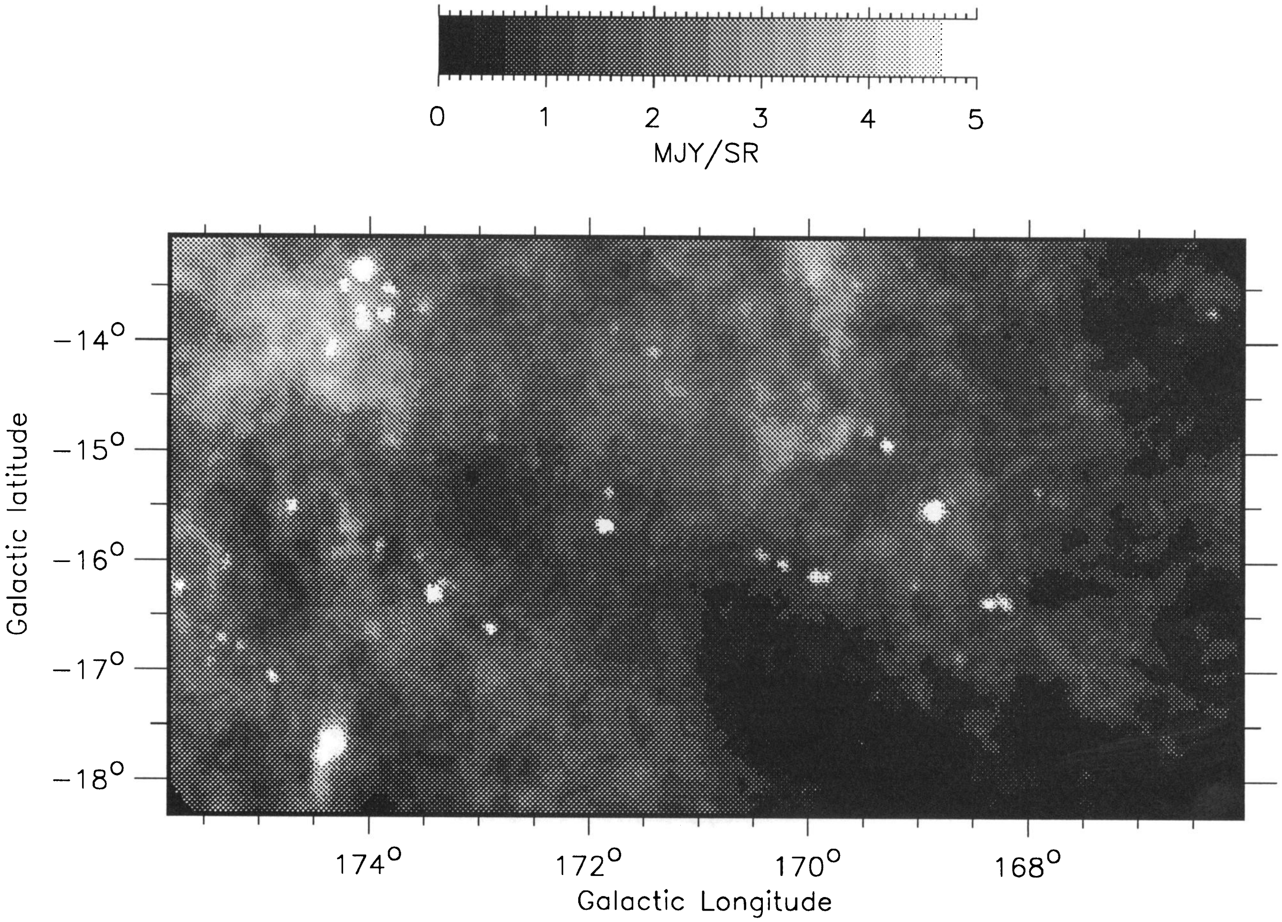

FIG. 4*b*

ABERGEL et al. (see 423, L60)

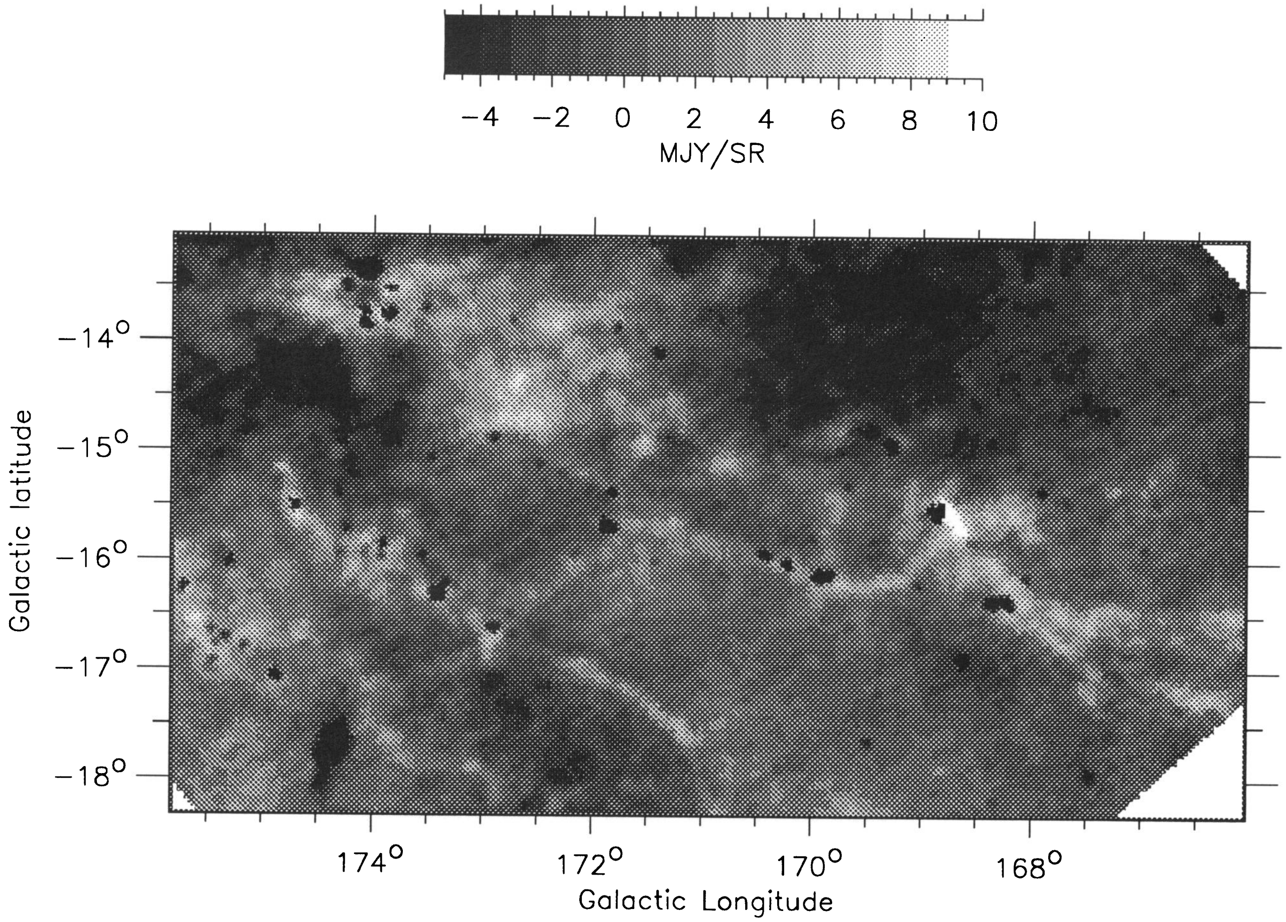

FIG. 5.—Cold component of the dust emission image projected upon the same grid that the one of the ^{13}CO ($J = 1–0$) map (Fig. 3)

ABERGEL et al. (see 423, L60)

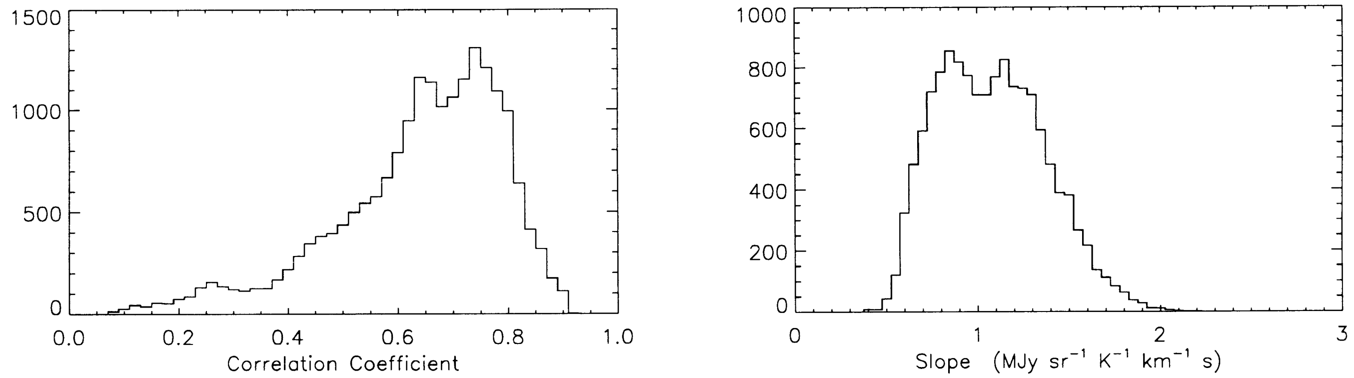

FIG. 7*a* FIG. 7*b*

FIG. 7.—Histogram analysis of the correlation coefficient (*a*) and the regression line slope (*b*) between the ^{13}CO ($J = 1$–0) velocity integrated emission and the cold component of the dust emission. In (*b*), only pixels with correlation coefficients greater than 0.6 are analyzed.

As the *IRAS* resolution is twice the ^{13}CO sampling, the number of independent pixels inside each box is equal to 110. The correlation coefficient (r) and the slope of the regression line between the two emissions are computed inside these small boxes centered on each observed pixel of the ^{13}CO map. The contributions of regions heated by faint sources is limited by eliminating pixels with negative cold component emissions. We have checked that this does not eliminate the cloud edges from the correlation analysis.

Computed inside these small boxes, the values of r are greater than 0.6 for 70% of the observed pixels (see the histogram analysis on Fig. 7*a*). Thus the small-scale correlation is significantly better than the correlation inside the whole map for 70% of the observed pixels. This result allows us to predict that the ^{13}CO ($J = 1$–0) emission should be detectable for at least 70% of the bright regions of the large-scale cold component map (Fig. 2).

Figure 8 (Plate L13) displays the values of the regression line slope between the two emissions received by pixels with $r > 0.6$. Differences of slope greater than 0.1 MJy sr^{-1} K^{-1} km^{-1} s are significant because they are visible on the raw data. Therefore we can consider this value as the uncertainty on the computed slopes. The histogram analysis (Fig. 7*b*) shows that the range of slope is very limited: the values are less than 0.8 MJy sr^{-1} K^{-1} km^{-1} s for 20% of the observed pixels, and greater than 1.4 MJy sr^{-1} K^{-1} km^{-1} s for 20% of them. This difference of a factor around 2 is significant, as the slope gradients are visible in Figure 8. Along the southern filament, the slope increases from east to west, from 1 to 1.9 MJy sr^{-1} K^{-1} km^{-1} s and then decreases up to 1.1 MJy sr^{-1} K^{-1} km^{-1} s. In the northern filament, the slope decreases from 0.8 to 0.6 MJy sr^{-1} K^{-1} km^{-1} s, and then slowly increases up to 1.4 MJy sr^{-1} K^{-1} km^{-1} s in an extended region lying to the west of the filament.

We should obtain the same values for the regression line slopes between the 100 μm (without removing the 60 μm emission) and the ^{13}CO emissions because within our small boxes there is no significant correlation between the 60 μm emission and the ^{13}CO emission. Inside B5, Langer et al. (1989) have found that the regression line slopes between the 100 μm emission and the integrated ^{13}CO ($J = 1$–0) emission are in the range 1.1–2.5 MJy sr^{-1} K^{-1} km^{-1} s. Inside HCL 2 and B18, Snell et al. (1989) have obtained, respectively, 2.22 ± 0.03 and 1.36 ± 0.03 MJy sr^{-1} K^{-1} km^{-1} s. We see that all the values of the slope between the 100 μm emission and the integrated ^{13}CO emission are in the same range, while obtained in different regions.

The correlation coefficient is less that 0.6 for about 30% of the observed pixels (Fig. 7*a*), which correspond to black regions within observed areas in Figure 8. The most extended region of low r value lies to the west of TMC 1. Cuts across this region show a strong excess of the cold component emission, while the ^{13}CO emission is irregular without any large-scale feature. Smaller regions with a low r value coincide with sources which are excluded from the analyzed boxes but disturb the correlation inside neighborhood regions.

4. INTERPRETATION AND DISCUSSION

^{13}CO and cold component of the dust emissions correlate very well, with a slope which is not seen to change strongly from region to region. We can show that the ^{13}CO ($J = 0$–1) and cold component emitting volumes are roughly comparable by converting independently the ^{13}CO and cold component emission into H$_2$ column densities (N_{H_2}). The observed ratio between the two emissions corresponds to the ratios of the conversion factors to N_{H_2}.

The simple model which assumes an homogeneous cloud and local thermal equilibrium (LTE) conditions and the large velocity gradient (LVG) model developed by Castets et al. (1990) are both used to compute N_{H_2} from $I(^{13}\mathrm{CO})$ (Fig. 9). Studies of the excitation of CO and isotopes by Falgarone, Phillips, & Walker (1991) strongly suggest that the ^{13}CO emission of molecular clouds comes from cold ($T = 10$ K) dense gas ($n = 10^4$ cm^{-3}). We have assumed that the kinetic temperature is equal to 10 K, the ^{13}CO abundance 2×10^{-6} (Dickman 1978), the velocity width 1 km s^{-1}. For the LVG model, the calculations are made with two values of the molecular hydrogen density: 10^3 and 10^4 cm^{-3}. We see on Figure 9 that the values of N_{H_2} obtained from the homogeneous LTE model are ~1.5 to 2 times smaller that the ones obtained from the LVG model.

Direct comparisons of 100 μm images of clouds with extinction measurements provide an empirical calibration of the ratio $I_\nu(100)/A_v$ between 5 and 10 MJy sr^{-1} mag^{-1} for clouds with less than 3 mag of extinction (Boulanger 1989). Models of radiative transfer and infrared emission of dust (Bernard et al. 1992) lead to similar values and show how this ratio decreases for clouds with larger extinctions. Figure 9 of Bernard et al. (1992) gives relation between the 100 μm emission and hydrogen column density for a set of their models. Comparing our

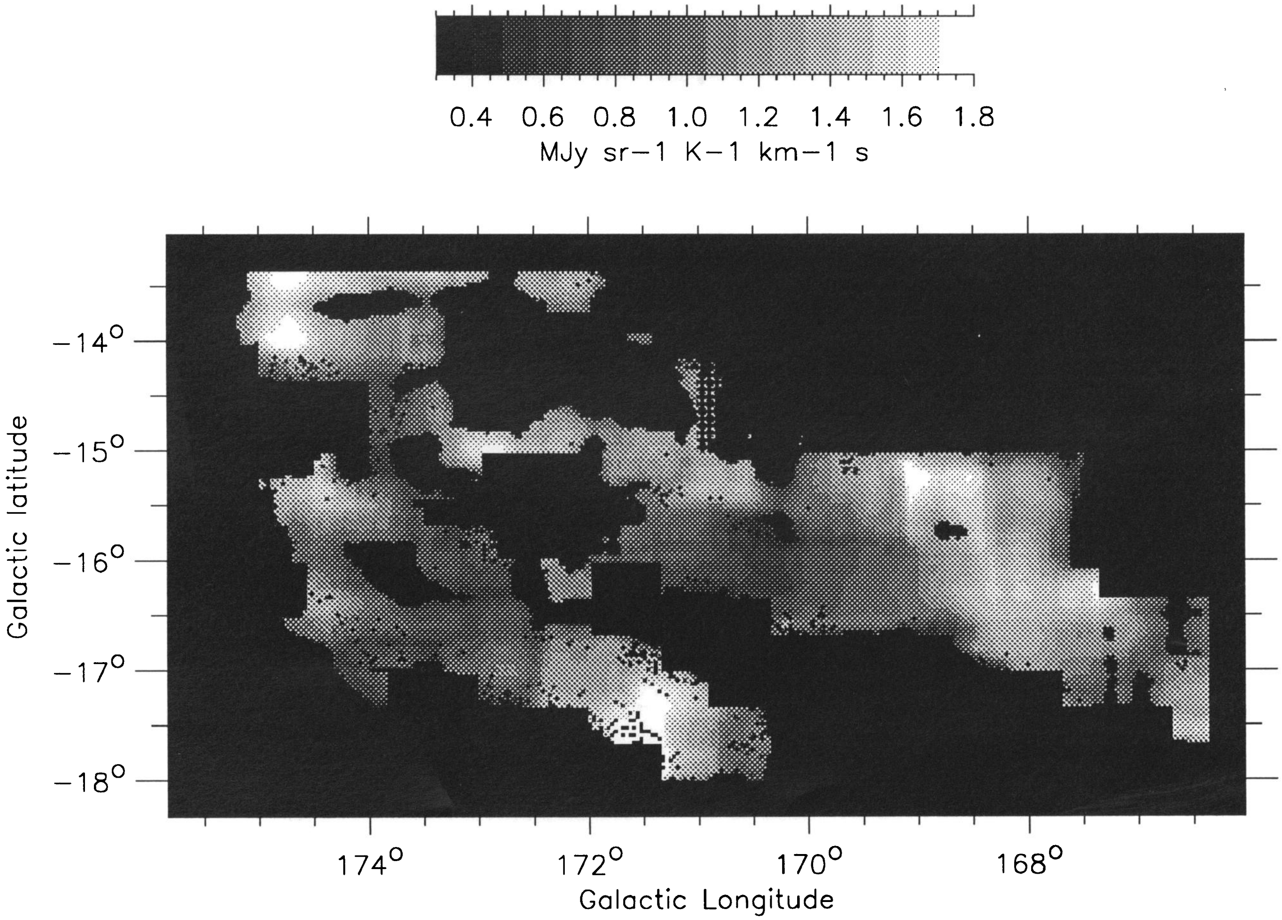

FIG. 8.—Values of the regression line slope between the ^{13}CO (J = 1–0) velocity integrated emission and the cold component of the dust emission. Only pixels with correlation coefficients greater than 0.6 are displayed.

ABERGEL et al. (see 423, L61)

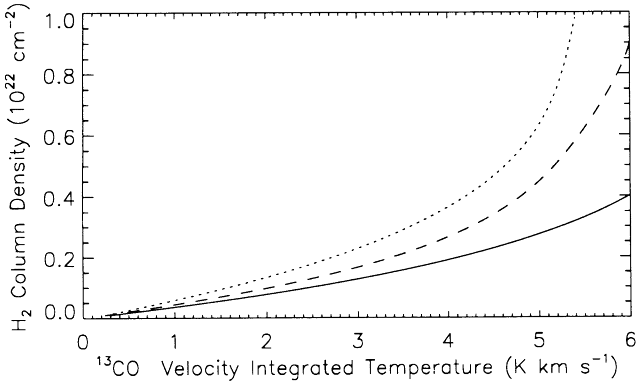

FIG. 9.—Computed value of N_{H_2} as a function of the ^{13}CO antenna temperature for the homogeneous and LTE model (*solid line*), and the LVG model developed by Castets et al. (1990) with a molecular hydrogen density equal to 10^3 and 10^4 cm^{-3} dotted and dashed lines, respectively). We have assumed that the kinetic temperature is equal to 10 K, the ^{13}CO abundance 2×10^{-6} (Dickman et al. 1978), and the velocity width 1 km s^{-1}.

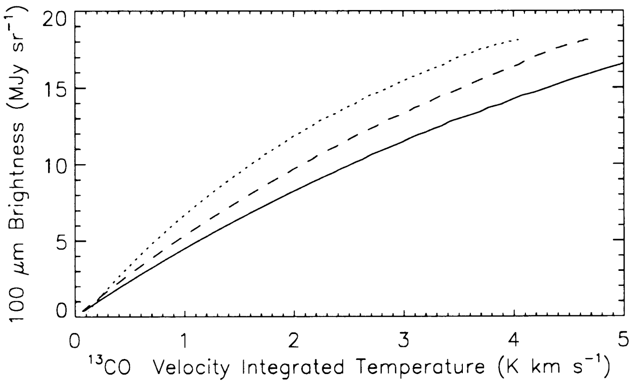

FIG. 10.—Relationship between the 100 μm emission and the ^{13}CO (J = 0–1) antenna temperature computed using the homogeneous LTE model (*solid line*), and the LVG model with a molecular hydrogen density equal to 10^3 and 10^4 cm^{-3} (*dotted and dashed lines*, respectively). N_{H_2} is converted into 100 μm emission using Fig. 9 of Bernard et al. (1992), assuming that the total visible extinction toward the center of the cloud is equal to 4 mag. This maximal extinction corresponds to a value of the 100 μm emission equal to 18 MJy sr^{-1}.

Figure 9 and Figure 9 from Bernard et al. one may see that the relations $I(^{13}\mathrm{CO})$–N_{H_2} and $I_\nu(100)$–N_{H_2} level off for comparable column densities (a few 10^{21} cm^{-2}). This is illustrated by Figure 10 where we have combined the two relationships $I(^{13}\mathrm{CO})$–N_{H_2} and $I_\nu(100)$–N_{H_2} (assuming that the total visible extinction toward the center of the cloud is equal to 4 mag) into a $I(^{13}\mathrm{CO})$–$I_\nu(100)$ diagram. We see that the saturation of the two emissions is no more visible, which confirms that these two emissions trace a comparable depth in molecular clouds. One may be cautious in comparing the relation in Figure 10 with the observed correlation I(cold)–$I(^{13}\mathrm{CO})$. First, the cold IR component is usually embedded in matter with warm IR color which contributes to the total 100 μm emission. In the same way, the ^{13}CO emission (Fig. 9) may start rising above some nonzero H$_2$ column density. Second, when computing I(cold) by subtracting the 60 μm from the 100 μm image, some of the 100 μm emission from the cold component is removed.

It is clear from Figure 10 that, for the models we have used, similar column densities are necessary to account for the ^{13}CO and 100 μm brightnesses. The fact that the three curves on Figure 10 are not very different shows that the choice of the model used to convert the velocity-integrated ^{13}CO (J = 1–0) emission into N_{H_2} does not seem critical. The differences seen in between the three models in Figure 9 does not appear as clearly in Figure 10 because the dependence of $I(^{13}\mathrm{CO})$ and $I_\nu(100)$ on N_{H_2} is less than linear. Thus, to affect the slope of the $I_\nu(100)$–$I(^{13}\mathrm{CO})$ correlation, the relation between $I(^{13}\mathrm{CO})$ or $I_\nu(100)$ with N_{H_2} must be modified to a higher degree.

The variations of a factor of 2 of the values of the regression line slope between the far-infrared and ^{13}CO emissions have to be studied. They should result from different physical properties of the dust (emissivity of the big grains) and differences in ^{13}CO abundance, excitation and radiation transfer conditions, in particular cloud clumpiness and velocity structure (which can be analyzed from the observed ^{13}CO lines). These differences may occur inside the complex within distances as small as our analysis box, i.e., 0.9 pc.

REFERENCES

Abergel, A., et al. 1994, in preparation
Beichman, C. A., Boulanger, F., & Moshir, M. 1992, ApJ, 386, 248
Bernard, J. P., Boulanger, F., Désert, F. X., & Puget, J. L. 1992, A&A, 263, 258
Boulanger, F. 1989, The Physics and Chemistry of Interstellar Molecular Clouds, ed. G. Winnewisser & J. T. Armstrong (Berlin: Springer)
Boulanger, F., Falgarone, E., Puget, J. L., & Helou, G. 1990, ApJ, 364, 136
Boulanger, F., & Pérault, M. 1988, ApJ, 330, 964
Castets, A., Duvert, G., Dutrey, A., Bally, J., Langer, W. D., & Wilson, R. W. 1990, A&A, 234, 469
Cernicharo, J., & Guélin, M. 1987, A&A, 176, 299
Désert, F. X., Boulanger, F., & Puget, J. L. 1990, A&A, 237, 215
Dickman, R. L. 1978, ApJS, 37, 407
Elias, J. H. 1978, ApJ, 224, 857
Falgarone, E., Phillips, T. G., & Walker, C. K. 1991, ApJ, 378, 186
Fukui, Y., & Mizuno, A. 1991, in IAU Symp. 147, Fragmentation of Molecular Clouds and Star Formation, ed. E. Falgarone, F. Boulanger, & G. Duvert (Dordrecht: Kluwer), 275
Langer, W. D., Wilson, R. W., Goldsmith, P. F., & Beichman, C. A. 1989, ApJ, 337, 355
Laurejis, R. J., Clark, F. O., & Prusti, T. 1991, ApJ, 372, 185
Nercessian, E., Castets, A., Cernicharo, J., & Benayoun, J. J. 1988, A&A, 189, 207
Sykes, M. V. 1988, ApJ, 334, L55
Snell, R. L., Heyer, M. H., & Schloerb, F. P. 1989, ApJ, 337, 739
van Dishoeck, E. F., & Black, J. H. 1988, ApJ, 334, 771
Viala, Y. P., Letzelter, C., Eidelsberg, M., & Rostas, F. 1988, A&A, 193, 265